Journal of Materials Chemistry A

Revealing Effect of Interfacial Electron Transfer in Heterostructured Co9S8@NiFe LDH for Enhanced Electrocatalytic Oxygen Evolution

Journal:	*Journal of Materials Chemistry A*
Manuscript ID	TA-ART-03-2021-002318.R2
Article Type:	Paper
Date Submitted by the Author:	28-Apr-2021
Complete List of Authors:	Feng, Xueting; Beijing Institute of Technology Jiao, Qingze; Beijing Institute of Technology, School of Chemical Engineering and Environment Dai, Zheng; Beijing Institute of Technology Dang, Yanliu; University of Connecticut Suib, Steven; University of Connecticut, U-60, Department of Chemistry Zhang, Jiatao; Beijing Institute of Technology, School of Materials Science and Engineering Zhao, Yun; Beijing Institute of Technology, School of Chemical Engineering and the Environment Li, Hansheng; Beijing Institute of Technology Feng, Caihong; Beijing Institute of Technology, School of Chemical Engineering and Environment Li, Anran; Beihang University, Beijing Advanced Innovation Center for Big Data-Based Precision Medicine

ARTICLE

Revealing Effect of Interfacial Electron Transfer in Heterostructured Co_9S_8@NiFe LDH for Enhanced Electrocatalytic Oxygen Evolution

Received 00th January 20xx,
Accepted 00th January 20xx

DOI: 10.1039/x0xx00000x

Xueting Feng,[a, d] Qingze Jiao,[a, c] Zheng Dai,[a] Yanliu Dang,[e] Steven L. Suib,[d, e] Jiatao Zhang,[a] Yun Zhao,[a] Hansheng Li,[a] Caihong Feng,*[a] and Anran Li,*[b]

Heterointerface engineering is a desirable way to rationally design efficient and low-cost electrocatalysts for the oxygen evolution reaction (OER). Herein, the urchin-like Co_9S_8@NiFe layered double hydroxide (Co_9S_8@NiFe LDH) heterostructured hollow spheres are assembled by Co_9S_8 hollow spheres as core and porous NiFe LDH nanowires as shells. The heterostructured hollow spheres show a small overpotential of 220 mV at a current density of 10 mA cm^{-2}, a low Tafel slope of 52.0 mV dec^{-1}, and robust stability, which is better than that of commercial IrO_2 and most reported non-precious electrocatalysts. Density functional theory (DFT) calculations show that the synergetic effect at the interface could improve the electrical conductivity of Co_9S_8@NiFe LDH, induce electron transfer from NiFe LDH to Co_9S_8, and lower energy barriers of the intermediates for OER, leading to enhanced electrocatalytic activity. Meanwhile, the urchin-like hollow structure with nanopores and super-hydrophilicity can provide desired structural stability, facilitate ion penetration and release of bubbles, improving the accessibility of active sites, and thereby boosting OER catalytic performance. This work provides a viable route to develop high performance electrocatalysts for the OER.

Introduction

The Electrocatalytic water splitting, converting electricity into hydrogen energy, represents a sustainable approach for hydrogen generation from aqueous solutions.[1] This process includes two half reactions, the oxygen evolution reaction (OER) and the hydrogen evolution reaction (HER).[2] Due to the sluggish kinetics of the four-electron process, the OER, considered as the rate-determining step, usually needs catalysts to decrease the reaction energy barrier.[3] Currently, Ir/Ru-based oxides are used as commercial OER electrocatalysts, while scarcity, high cost, and poor stability hamper their extensive industrial application.[4] Thus, it is crucial to explore highly efficient and non-precious metal catalysts.

Recently, transition metal sulfides (TMS), especially cobalt based sulfides, possessing low cost, and superior electrocatalytic performances to their counterpart oxides, have been regarded as promising noble metal candidate substitutes for OER.[5] Among them, cubic Co_9S_8 demonstrates excellent OER performance owing to its remarkable redox capability.[6] Generally, TMS would be converted to transition metal oxides/(oxy)hydroxides along with the leaching of S during the OER process in highly oxidizing conditions. This transformation is inevitably accompanied by the collapse of the structure and the transformation of compositions, leading to inferior catalytic activity and poor stability towards OER.[7] To overcome these disadvantages, both experimental and theoretical studies have indicated that regulation of electronic structure can greatly increase active sites, tune the local electronic structure of the metal centers, and lower energy barriers of OER intermediates via chemical composition modification of electrocatalysts and construction of heterogeneous nanostructures by surface/interface engineering.[8-11] Recently, NiFe layered double hydroxide (NiFe LDH) has attracted attention due to its flexible chemical composition, enhanced resistance of degradation, and excellent catalytic activity toward OER.[12,13] Meanwhile, by combining NiFe LDH with conductive materials, the interfacial electronic structures will change and promote OER activity.[14] Therefore, many efforts have been devoted to integrating NiFe LDH with other materials to construct biphasic composites for achieving high electrocatalytic activity.[15] In this context, Feng et al. reported that introducing NiFe-LDH into $Co_{0.85}Se$, with strong coupling effects, could improve the catalytic activity for overall water splitting.[16] Wang et al. verified that the interfaces of NiO and NiFe LDH could create new active sites compared to pure NiO, leading to optimized OER performance.[17] Xu et al. showed that the deposition of NiFe LDH on Co_3O_4 could modulate the

---

[a] Beijing Key Laboratory for Chemical Power Source and Green Catalysis, School of Chemistry and Chemical Engineering, Beijing Institute of Technology, Beijing 100081, People's Republic of China.
[b] Beijing Advanced Innovation Center for Big Data-Based Precision Medicine, School of Engineering Medicine, Beihang University, Beijing 100191, People's Republic of China.
[c] School of Materials and Environment, Beijing Institute of Technology, Jinfeng Road No.6, Xiangzhou District, Zhuhai 519085, People's Republic of China.
[d] Department of Chemistry, University of Connecticut, U-3060, 55 N. Eagleville Road, Storrs, Connecticut 06269, United States.
[e] Institute of Materials Science, University of Connecticut, U-3136, 97 N. Eagleville Road, Storrs, Connecticut 06269, United States.

Electronic Supplementary Information (ESI) available: [details of any supplementary information available should be included here]. See DOI: 10.1039/x0xx00000x

interfacial cation chemical valences by changing electronic absorption and/or donor effects, and then boosted the OER electrocatalytic activity.[18]

In addition, nanostructured strategies can dramatically improve electrochemical properties. On one hand, hierarchical hollow nanostructures with hydrophilic structures and high specific surface areas (SSA) can facilitate the access of reactants and release of bubbles from the catalyst surfaces, which is beneficial to the OER performance of electrocatalysts.[19] In particular, the spherical morphology composed of nanowires possesses roughness at the micro/nano scales, and such structures can not only provide a strong capillary force to pump liquid, but also generate desired structural stability.[20] On the other hand, the heterointerface created by different active materials can lead to abundant exposed active sites and efficient interfacial charge transfer.[21] Inspired by the above concepts, it is highly desirable to enhance the OER performance by constructing Co_9S_8@NiFe LDH composites with porous urchin-like hollow structures.

Herein, porous urchin-like Co_9S_8@NiFe LDH heterostructured hollow spheres were designed and fabricated using Co_9S_8 hollow spheres as a scaffold. The detailed analyses demonstrated that the strong electronic interactions between Co_9S_8 and NiFe LDH could enhance their electronic conductivity and reduce the reaction energy barrier, and thus boost their catalytic activity. The unique urchin-like hollow spheres with super-hydrophilicity can facilitate the access of reactants and release of bubbles from the surface of catalysts. Due to the high SSA, surper-hydrophilicity, and electronic interactions between NiFe LDH and Co_9S_8, the Co_9S_8@NiFe LDH showed superb OER activity in 1 M KOH. This system delivered a current density of 10 mA cm^{-2} with a low overpotential of 220 mV and Tafel slope of 52.0 mV dec^{-1}, which is superior to Co_9S_8 (282 mV, 57.7 mV dec^{-1}), NiFe LDH (342 mV, 89.0 mV dec^{-1}) and commercial IrO_2 (341 mV, 91.6 mV dec^{-1}).

Experimental section

Synthesis of Co_9S_8@NiFe LDH

The Co_9S_8 hollow spheres were prepared as in our previous work.[22] The urchin-like Co_9S_8@NiFe LDH heterostructured hollow spheres were synthesized via a simple hydrothermal reaction. Typically, $Fe(NO_3)_3•9H_2O$ (0.202g, 0.5 mmol), $Ni(NO_3)_2•6H_2O$ (0.436g, 1.5 mmol) and urea (0.300g, 5 mmol) were dissolved into distilled water (50 mL) stirring for 10 min and then Co_9S_8 hollow spheres (0.180 g) were introduced, stirring for another 1 h. Subsequently, the resultant solution was transferred into a 75 mL Teflon-lined stainless-steel autoclave and kept at 120 °C for 10 h in a continuous stirring oven. Finally, the samples were washed by water and ethanol, and dried at 60 °C for 12 h.

For comparison, NiFe LDH nanowires were synthesized via the above processes without adding Co_9S_8 hollow spheres.

Materials characterization

An X-ray diffractometer (XRD, Rigaku) with Cu Kα radiation was used to analyze the phase structures of the materials. Scanning electronic microscopy (SEM, JEOL JSM-7500F), transmission electronic microscopy (TEM), and high-resolution TEM (HRTEM, Hitachi HT7700) were used to identify the morphologies of the materials. High-angle annular dark-field scanning transmission electron microscopy (HAADF-STEM) images and energy dispersive X-ray spectrum (EDS) were collected using a Talos F200X microscope operating at 200 kV. X-ray photoelectron spectroscopy (XPS, PHI QUANTERA-II SXM) was used to examine the surface chemical state of the materials. The Brunauer-Emmett-Teller (BET) experiments were performed by nitrogen adsorption/desorption measurements collected on an ASAP2020 instrument. The hydrophilicity presented by the water contact angles (a droplet with a rate of 1 μL s^{-1} and volume of 2 μL) was tested using a contact angle goniometer (Data-Physics OCA-15E, Germany). Inductively coupled plasma mass spectrometry (ICP-MS) analysis was performed on Thermo ICAP-Q.

Electrochemical measurements

The electrocatalytic performance of OER was conducted by a potentiostat (CHI760e, CH Instruments) with a rotating disk electrode (RDE) in a three-electrodes system. In 1 M KOH, a glass carbon (GC) electrode (5 mm in diameter) decorated with catalyst, platinum wires and Hg/HgO (1 M KOH) electrode were used as the working, the counter and the reference electrode, respectively. To reduce the influence of Fe on the OER activity, we followed the procedures reported by Burke et al. to scavenge Fe ions in the electrolyte solution.[23] The ICP-MS was used to monitor the amount of Fe in 1 M KOH. After purification, the amount of Fe is only 73.92 ppb. The preparation of catalyst ink was shown in Supplementary Information. Linear sweep voltammogram (LSV), corrected with *iR*-compensation, was carried out in 1.2-1.9 V vs. RHE with a scan rate of 5 mV s^{-1} at 1600 rpm. The double-layer capacitance (C_{dl}) was determined using cyclic voltammetry (CV) at various scan rates (2, 4, 6, 8, 10 mV s^{-1}) in a non-faradaic region to analyze the electrochemically active surface area (ECSA). The ECSA was calculated by the following equation,

$$\boldsymbol{ECSA = C_{dl}/C_S}$$

Where C_s represents the specific capacitance. The value of specific capacitance is 0.04 mF cm^{-2} in this calculation.[24,25]

The faradaic efficiency (ε) was checked by the rotating ring-disk electrode (RRDE) with a ring potential of 0.4 V vs. RHE and calculated by the equation,

$$\boldsymbol{\varepsilon = I_r/(I_d \times N)}$$

where I_r, I_d and N=0.37 are the ring current, disk current and collection efficiency, respectively. The accelerated stability and long-term stability of catalysts were assessed by CV for 1000 cycles at a scan rate of 100 mV s^{-1} and chronoamperometric response with an overpotential of 220 mV for 20 h. The electrochemical impedance spectroscopy (EIS) was performed between 0.01 Hz and 100 kHz with an AC amplitude of 5 mV at 1.45 V.

All potentials in this work were calibrated to RHE by following equation,

$$\boldsymbol{E_{RHE} = E_{(Hg/HgO)} + 0.0591 \times pH + 0.098}$$

Theoretical calculations

The Spin-polarized density functional theory (DFT) computations are carried out using the Vienna ab initio simulation package (VASP v.5.4.1) to reveal the interaction between the Co_9S_8 and the Ni_3Fe LDH.[26,27] The generalized gradient approximation (GGA) and the projector augments wave (PAW) pseudopotentials with the exchange and correlation in the Perdew-Burke-Ernzerhof (PBE) are employed to describe the ion-electro interaction.[28,29] The DFT + U technique is applied to the Ni, Co, and Fe atoms, where the U-J parameters for Ni, Co, and Fe 3d states are set to be 3.8 eV, 3.32 eV, and 4.3 eV, respectively.[30,31] For all calculations, a cut-off energy of 500 eV is used for the plane wave basis set to ensure convergence. The convergence threshold is set as 10-5 eV in energy and 0.04 eV Å^{-1} in force, respectively. The slab models with a 20 Å thick vacuum layer added along the z direction are constructed to model the (111) surfaces of Co_9S_8 and the (001) surfaces of Ni_3Fe LDH. The heterogeneous interface model of the (111) Co_9S_8@ (001) NiFe LDH with the lattice parameter of a=b=13.37 Å is then built with a small lattice mismatch of about 5%. The Van der Waals interaction in the Co_9S_8@NiFe LDH heterostructure is included by the DFT-D3 method.[32] To model the OER processes, the (012) surface is cleaved for the Co_9S_8@NiFe LDH heterostructure and NiFe LDH, respectively. For all calculations, the Monkhorst-Pack Gamma-centered k-points mesh is adopted where the spacing of uniformly sampled k points for each simulation is set to be no larger than 2π*0.02Å^{-1}. All structures are visualized using the program VESTA.[33]

Results and discussion

Fabrication and structural characterization

As shown in Fig. 1a, the urchin-like Co_9S_8@NiFe LDH heterostructured hollow spheres were obtained via a hydrothermal reaction. Firstly, the Co_9S_8 hollow spheres were synthesized through our previous work,[22] and the shell consisted of numerous particles (Fig. S1). The hydrophilic nature of the Co_9S_8 hollow spheres enables the Fe^{3+}, Ni^{2+}, and urea in the solution to cover the hollow spheres uniformly.[34] Then, Fe^{3+} and Ni^{2+} ions gradually hydrolyze to form porous NiFe-LDH nanowires and deposit onto the surface of Co_9S_8 hollow spheres, in which the Co_9S_8 hollow spheres serve as the skeleton offering copious nucleation sites for the adsorption of Ni^{2+} and Fe^{3+} ions followed by in-situ formation of NiFe LDH nanowires.

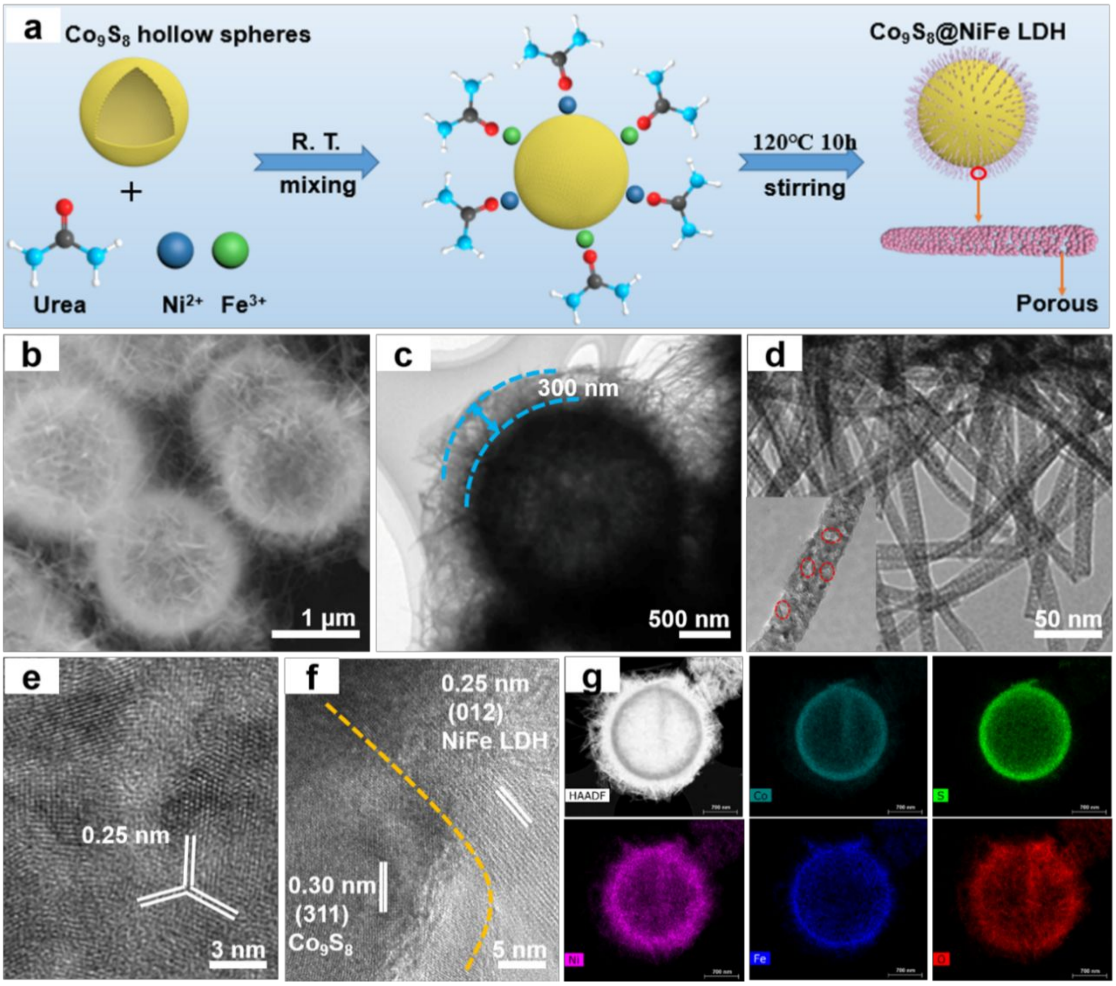

Fig. 1 (a) Schematic diagram for the synthetic process of the Co_9S_8@NiFe LDH. (b) SEM image of the Co_9S_8@NiFe LDH. (c) TEM image of the Co_9S_8@NiFe LDH. (d) TEM images and (e) HRTEM image of the NiFe LDH nanowires in the Co_9S_8@NiFe LDH. (f) HRTEM image of the Co_9S_8@NiFe LDH. (g) HAADF-STEM image and EDS mapping of Co, S, Ni, Fe, and O.

The SEM image in Fig. 1b shows that Co_9S_8@NiFe LDH with a diameter of approximately 2.6 µm is made of high-quality urchin-like microspheres consisting of uniform NiFe LDH nanowires attaching on the Co_9S_8 hollow spheres to achieve a hierarchical heterostructure. In contrast with highly distributed urchin-like Co_9S_8@NiFe LDH microspheres, pure NiFe LDH nanowires are randomly interconnected and are inclined to aggregate (Fig. S2). TEM was performed to further observe the detailed structure and morphology of Co_9S_8@NiFe LDH. As shown in Fig. 1c, the afore-mentioned sample possesses a core-shell structure, which consists of aligned nanowires with a vertical size of 300 nm and a width of 15-20 nm (Fig. 1d) and a hollow core with a dimeter of 2 µm. The selected area electron diffraction (SAED) pattern of NiFe LDH nanowires in Co_9S_8@NiFe LDH (Fig. S3) illustrates its polycrystalline nature with rings corresponding to (101), (015) and (110) planes of NiFe LDH. Importantly, each individual nanowire is assembled from numerous connected particles and possesses many nanopores which may ascribe to the production of CO_2 during the process of urea hydrolysis (the inset of Fig. 1d).[35,36] The corresponding HRTEM image of NiFe LDH nanowire in Fig. 1e clearly presents the hexagonal symmetry of NiFe LDH with lattice dimensions of 0.25 nm. In addition, the HRTEM image of the Co_9S_8@NiFe LDH shows an apparent interface between the (311) planes of Co_9S_8 and the (012) planes of NiFe LDH (Fig. 1f). The EDS mapping (Fig. 1g and Fig. S4) and line scan result (Fig. S5) of the Co_9S_8@NiFe LDH further demonstrate the core-shell structure and phase boundaries, in which Ni, Fe, and O are distributed throughout the shell structure, while Co and S are homogeneously distributed in the central spheres.

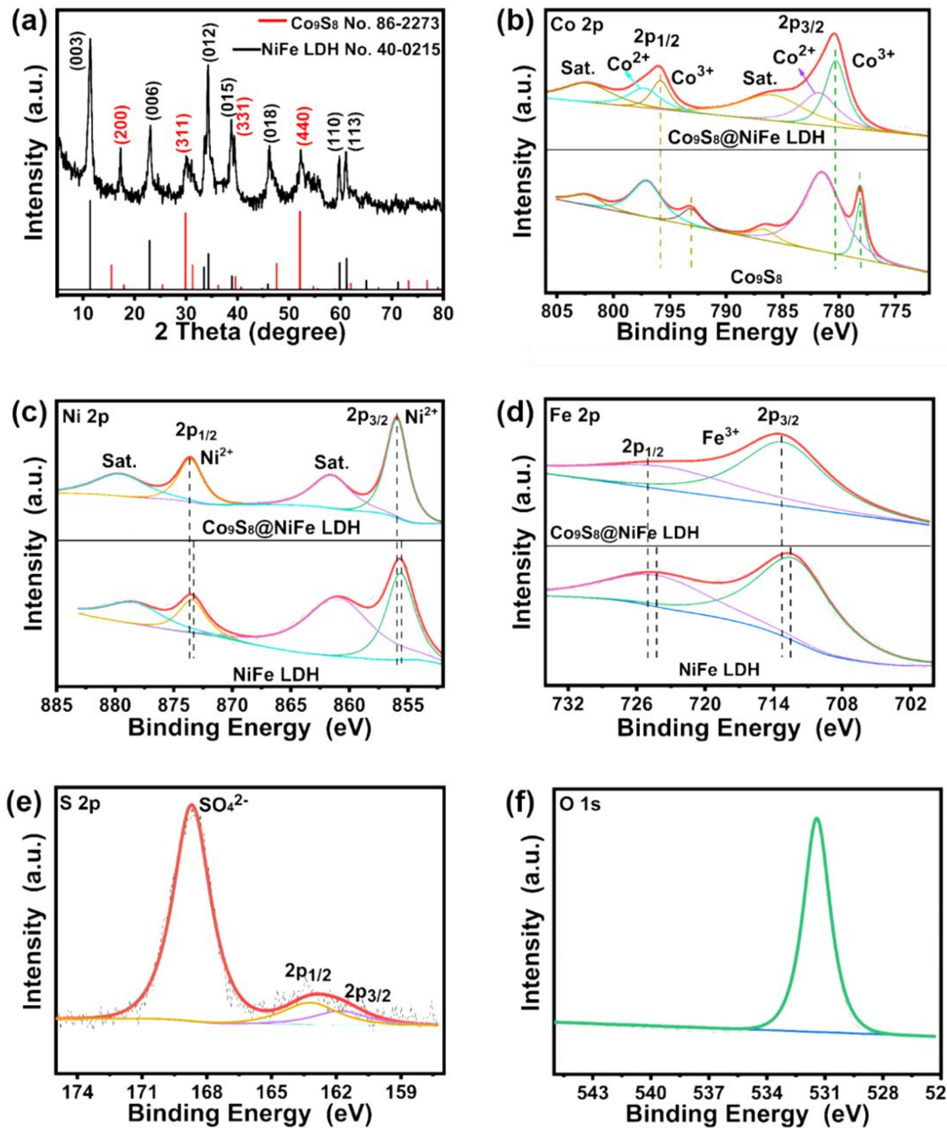

Fig. 2. (a) XRD pattern of Co_9S_8@NiFe LDH. (b) High-resolution XPS spectra of Co 2p in Co_9S_8@NiFe LDH and Co_9S_8. High-resolution XPS spectra of (c) Ni 2p and (d) Fe 2p in Co_9S_8@NiFe LDH and NiFe LDH. High-resolution XPS spectra of (e) S 2p and (f) O 1s in Co_9S_8@NiFe LDH.

The XRD pattern in Fig. 2a shows that the peaks at 17.8°, 29.8°, 39.5° and 52.1° correspond to the (200), (311), (331), (440) planes of Co_9S_8 (JCPDS No. 86-2273), respectively, and the other peaks are attributed to NiFe LDH (JCPDS No. 40-0215). This suggests the successful formation of Co_9S_8@NiFe LDH. XPS was performed to investigate the chemical state of Co_9S_8@NiFe LDH, pure Co_9S_8, and NiFe LDH. As shown in Fig. 2b, the peaks at 780.9/796.4 eV and 782.4/797.9 eV for Co 2p spectra of Co_9S_8@NiFe LDH correspond to Co^{3+} and Co^{2+}.[37] Compared to pure Co_9S_8, the binding energies of both Co $2p_{3/2}$ and Co $2p_{1/2}$ shift to high values, suggesting electrons being transferred to Co_9S_8 due to heterointerface engineering. In the Ni 2p spectra (Fig. 2c), the peaks at 855.8 and 873.4 eV are assigned to Ni $2p_{3/2}$ and Ni $2p_{1/2}$, respectively, indicating the presence of Ni^{2+}.[38] The other peaks at 861.4 and 879.5 eV are attributed to satellite peaks. The comprehensive positive shifts of Ni $2p_{1/2}$ and Ni $2p_{3/2}$ reveal the electron-donating ability of Ni in Co_9S_8@NiFe LDH, resulting in higher valence states.[39] The Fe 2p spectra (Fig. 2d) shows that the peaks at 713.2 and 723.7 eV are assigned to Fe $2p_{3/2}$ and Fe $2p_{1/2}$, revealing that the valence of Fe is 3.[40] The obvious positive shifts of Fe species in comparison with pure NiFe LDH confirm the strong electronic interactions between Co_9S_8 hollow spheres and NiFe LDH nanowires at the heterointerface.[41] In the case of the S 2p spectrum (Fig. 2e), the peaks at 161.8 and 163.2 eV are assigned to S^{2-}, which suggests the formation of metal-S bonds.[42] The peak at 168.8 eV is assigned to SO_4^{2-}. The O 1s spectrum (Fig. 2f) exhibits a peak at 531.2 eV which corresponds to layered double hydroxide.[43] All these results show the strong electronic coupling between Co_9S_8 and NiFe LDH in the Co_9S_8@NiFe LDH heterostructure, which can affect the electron transfer behavior, tune the electronic structure of metal centers, and then lead to improvement of electrocatalytic performance.[44]

Fig. S6 shows the N_2 adsorption/desorption isotherms of the Co_9S_8@NiFe LDH and Co_9S_8. Clearly, both have a type IV classification, which is a typical mesoporous structure. A predominant peak with 9.8 nm for Co_9S_8@NiFe LDH was observed, further verifying its mesoporous structure. The SSA and the pore volume are estimated to be 89 m^2 g^{-1} and 0.544 cm^3 g^{-1} for Co_9S_8@NiFe LDH, which are much larger than those of Co_9S_8 with SSA of 66 m^2 g^{-1} and a pore size of 0.085 cm^3 g^{-1}. These results suggest that Co_9S_8@NiFe LDH has abundant pores and desirable surface areas, which can facilitate mass transfer and increase the access of active sites. Additionally, hydrophilicity of the catalysts is particularly important for OER activity. As presented in video 1, the contact angle of the Co_9S_8@NiFe LDH is difficult to be evaluated because of the immediate rupture of droplets when deposited on the surface of Co_9S_8@NiFe LDH, exhibiting surprising hydrophilicity. In contrast, Co_9S_8 possesses inferior hydrophilicity (video 2). The super-hydrophilicity, as well as the hierarchical structure with roughness at both the micro and nano scales, can effectively ameliorate the surface wettability and improve access of reactants and release of bubbles.[40,45] Zhang et al. reported that a nanoforest morphology showed better surface hydrophilicity than that of microspheres, and the hydrophilic surface can further result in aerophobic properties, leading to effective contact between water and electrocatalyst and the detachment of bubbles.[19] Therefore, Co_9S_8@NiFe LDH can be an efficient and robust electrocatalyst for OER.

Electrocatalytic performance for OER

The catalytic performance of Co_9S_8@NiFe LDH for OER was investigated using a three-electrode system in 1 M KOH. For comparison, the OER properties of the synthesized Co_9S_8, NiFe LDH, and commercial IrO_2 were also tested. Fig. 3a shows the LSV curves of all catalysts. As observed, the intense peaks at 1.34 V for Co_9S_8@NiFe LDH and 1.42 V for NiFe LDH are due to the oxidation of Ni^{2+} to Ni^{3+}.[46] Obviously, the Co_9S_8@NiFe LDH is highly active for OER and an overpotential of only 220 mV is needed to drive 10 mA cm^{-2}, which is superior to that of Co_9S_8 (282 mV), NiFe LDH (342 mV), and commercial IrO_2 (341 mV). The catalytic activity of Co_9S_8@NiFe LDH outperforms most reported single metal sulfides and NiFe LDH electrocatalysts in 1 M KOH, such as Co_9S_8 hollow microplates (278 mV),[47] cobalt sulfide nanosheets (312 mV),[48] ball-milled NiFe LDH (270 mV),[49] and single-layer NiFe LDH nanosheets (300 mV).[50] Also this material is better than several NiFe LDH-based nanocomposites and sulfide-based nanocomposites, such as NiO@NiFe LDH on nickel foam (NF) (265 mV),[51] N,S-rGO/WSe_2/NiFe LDH (250 mV),[52] and Ag_2S-CoS hetero-nanowires (275 mV).[53] This system is also superior to some hollow structured NiFe LDH-based nanocomposites and sulfide-based nanocomposites, such as (Co, Ni)Se_2@NiFe LDH hollow nanocages (277 mV),[54] NiFe LDH nanoplates/N-TiO_2 nanotube (235 mV),[55] hollow TiO_2@Co_9S_8 core-branch arrays (240 mV),[56] and hollow CeO_x/CoS hybrid nanostructure (269 mV).[57] More details are shown in Table S1. The corresponding Tafel plots in Fig. 3b show that the Tafel slope of Co_9S_8@NiFe LDH is 52.0 mV dec^{-1}, which is smaller than that of Co_9S_8 (57.7 mV dec^{-1}), NiFe LDH (89.0 mV dec^{-1}), and commercial IrO_2 (91.6 mV dec^{-1}), suggesting the Co_9S_8@NiFe LDH possesses favorable OER kinetics. The electrochemically active surface area (ECSA) was checked by electrochemical double-layer capacitances (C_{dl}) in 1 M KOH. The C_{dl} can be obtained via collecting CV data in the non-faradaic region from 2 to 10 mV s^{-1} (Fig. S7). The slopes of plots of $\Delta j/2 = (j_{anodic} - j_{cathodic})/2$ vs. scan rate are equal to C_{dl}.[58] As shown in Fig. 3c, the C_{dl} of Co_9S_8@NiFe LDH, Co_9S_8 and NiFe LDH are 31.8, 27.9, and 6.2 mF cm^{-2}, respectively, suggesting the Co_9S_8@NiFe LDH provides more exposed active sites and larger surface area. Moreover, the polarization curves normalized by ECSA (Fig. S8) further verify the intrinsic activity of the catalysts, which also exhibits the improved OER performance of Co_9S_8@NiFe LDH compared with Co_9S_8 and NiFe LDH. Furthermore, the faradaic efficiency of Co_9S_8@NiFe LDH was evaluated by RRDE measurements with a ring potential of 0.40 V. The setting of ring potential can ensure the observed current originates from the OER process. In Fig. 3d, the disk current remains at 430 μA (blue curve), and then the O_2 molecules sweep across the Pt ring electrode and are reduced. Thus, a ring current of 154 μA is obtained (black curve), which demonstrates that the recorded current catalysed by Co_9S_8@NiFe LDH is primarily ascribed to OER with a faradaic efficiency of 97-99%. The rapid electron transfer properties of catalysts are important for excellent OER performance. EIS measurements presented by the Nyquist plots are performed to further investigate the kinetics, and the results are shown in Fig. 3e. The fitting impedance parameters, R_s, R_{ct}, CPE_1, R_1 and CPE_2, denoted the resistance of the electrolyte solution, the charge transfer resistance, the constant phase element of the double layer, the resistance of the catalyst, and the constant

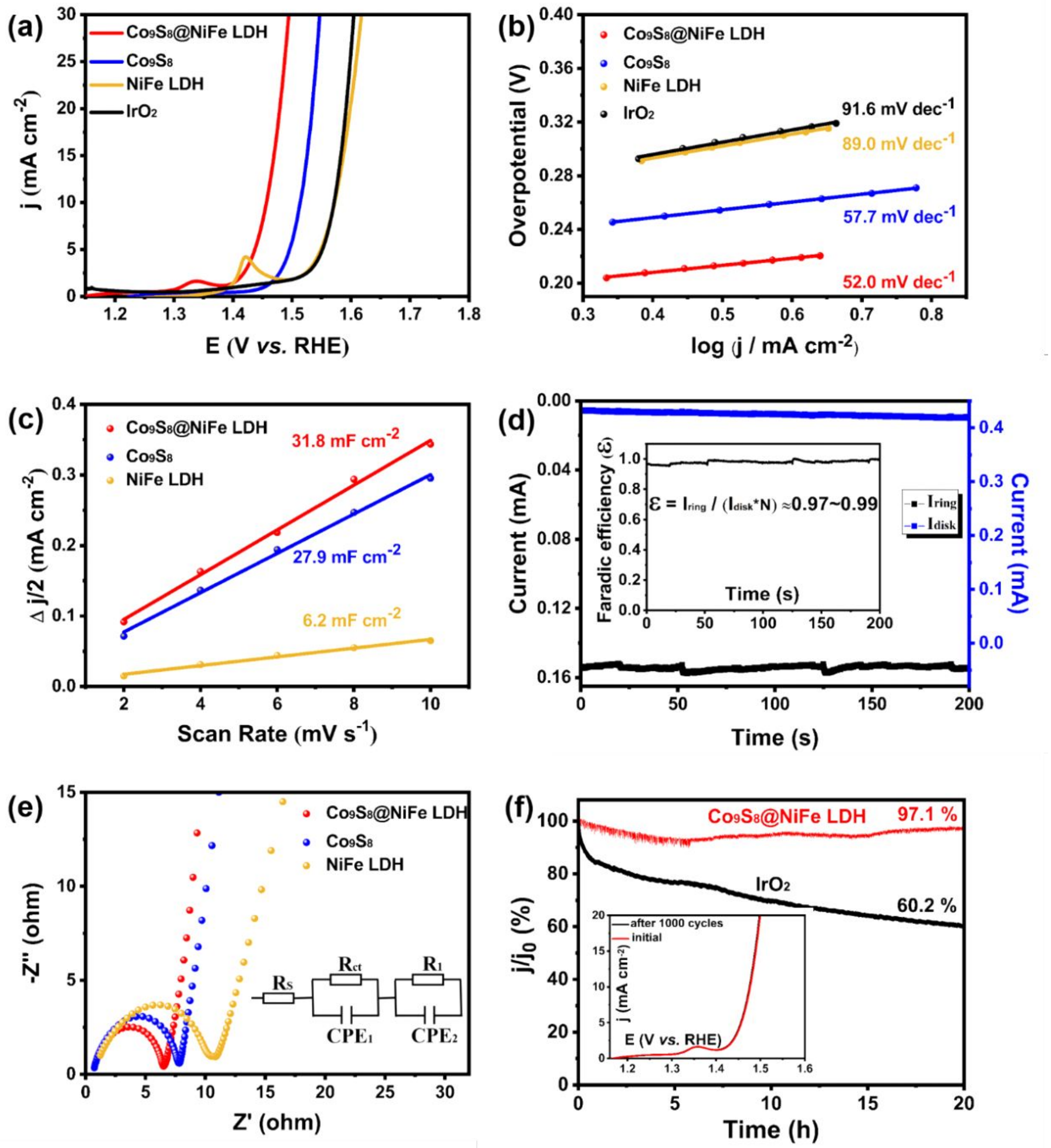

Fig. 3 (a) OER polarization curves and (b) Tafel plots of the Co_9S_8@NiFe LDH, Co_9S_8, NiFe LDH and IrO_2. (c) The plots of half of current density variation (j_{anodic}-$j_{cathodic}$) at 1.29 V *vs*. scan rate for the Co_9S_8@NiFe LDH, Co_9S_8 and NiFe LDH. (d) Disk and ring currents of Co_9S_8@NiFe LDH (inset: faradaic efficiency of Co_9S_8@NiFe LDH). (e) Nyquist plots and equivalent circuit of Co_9S_8@NiFe LDH, Co_9S_8 and NiFe LDH. (f) Stability of Co_9S_8@NiFe LDH at the overpotential of 220 mV, with accelerated stability inserted.

phase element of the catalyst layer, respectively.[59] All the elemental values were obtained from the fitted equivalent circuits and listed in Table S2 for the three samples. It is interesting to note that the similar R_s values indicate a consistent experimental configuration. The R_{ct} value of the Co_9S_8@NiFe LDH (5.87 Ω) is much smaller than that of Co_9S_8 (7.24 Ω) and NiFe LDH (9.96 Ω), suggesting its rapid charge transfer ability. Furthermore, the long-term stability and accelerated degradation tests of the Co_9S_8@NiFe LDH and commercial IrO_2 were studied in Fig. 3f. There is only 2.9 % degradation in the current density after 20 h stability test at an overpotential of 220 mV for Co_9S_8@NiFe LDH, which is superior to IrO_2 (39.8%). The accelerated degradation tests of the Co_9S_8@NiFe LDH were investigated by taking continuous CV data at 100 mV s^{-1} for 1000 cycles. Negligible change of the overpotentials at 10 mA cm^{-2} are observed before and after 1000 CV cycles (the inset of Fig. 3f), revealing the superior electrochemical stability for the Co_9S_8@NiFe LDH.

Characterizations of the Co_9S_8@NiFe LDH after stability testing

The chemical and structural stability of the Co_9S_8@NiFe LDH after 20-hrs stability tests were analyzed with XRD, XPS, SEM, TEM, HRTEM, and EDS. The XRD pattern of the Co_9S_8@NiFe LDH after 20-hrs stability tests for OER in Fig. 4a shows no obvious phase change compared with Co_9S_8@NiFe LDH before 20-hrs stability tests except for weakening of peak intensity. The corresponding XPS spectra of the Co_9S_8@NiFe LDH after 20-hrs stability tests for OER are presented in Fig. 4b-f. For the Co 2p spectra (Fig. 4b), the Co^{3+}/Co^{2+} ratios are 1.28 and 1.18 for the Co_9S_8@NiFe LDH after and before 20-hrs stability tests, respectively, and the difference is small. This suggests a mild superficial oxidation on the surface of Co_9S_8@NiFe LDH. For the Ni 2p transition (Fig. 4c), the peaks at 857.1 and 874.5 eV are ascribed to Ni^{3+} in NiOOH, suggesting partial oxidation of Ni^{2+} to Ni^{3+} and formation of NiOOH on the surface of NiFe LDH in Co_9S_8@NiFe LDH.[41] Compared with the Fe 2p spectrum before stability tests, the valence of Fe species is not changed after 20-hrs stability tests, and the peaks at 713.7 and 723.7 eV are assigned to Fe^{3+} (Fig. 4d).[40] The S 2p spectrum (Fig. 4e) shows that the peaks at 161.3 and 162.6 eV are assigned to S^{2-}, indicating that metal-S bonds still exist.[60] However, metal-S bonds of the pristine Co_9S_8 disappeared after the OER process (Fig. S9). The slight oxidation on the surface of Co_9S_8@NiFe LDH is also confirmed by the O 1s spectrum (Fig. 4f). The peaks at 531.2 eV and 531.7 eV belong to layered double hydroxide and NiOOH.[43,61] These results demonstrate that constructing NiFe LDH on the surface of Co_9S_8 to form heterostructures can effectively decrease surface oxidation of the Co_9S_8 in the Co_9S_8@NiFe LDH, and thus possess excellent chemical stability. The SEM image of Co_9S_8@NiFe LDH in Fig. 5a shows that the hollow structure keeps the original features quite well, while the hollow structure of pure Co_9S_8 tends to collapse (Fig. S10a). As shown in the TEM images (Fig. 5b-c), Co_9S_8@NiFe LDH retains the urchin-like hollow spherical morphology with NiFe LDH nanowires firmly attached on the Co_9S_8 hollow spheres, which supports the structural stability. In contrast, the morphology of Co_9S_8 is changed, and a few nanosheets appear on the surface of Co_9S_8 (Fig. S10b). The polycrystalline rings in the SAED pattern of NiFe LDH nanowires in the Co_9S_8@NiFe LDH (the inset of Fig. 5c) correspond to (101), (015), and (110) planes of NiFe LDH, confirming that the crystal structure of NiFe LDH in the Co_9S_8@NiFe LDH is maintained after 20-hrs stability tests.

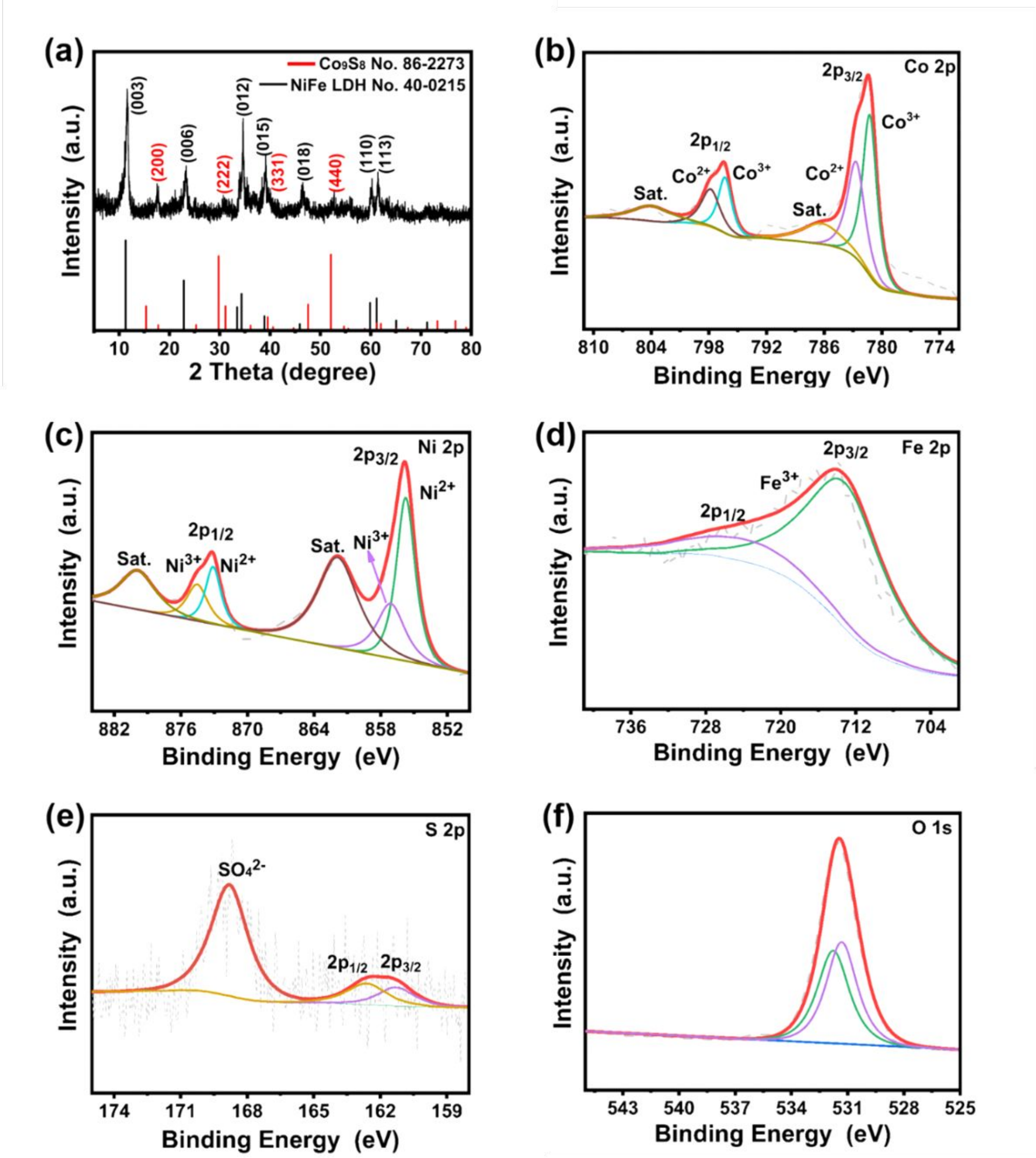

Fig. 4 (a) XRD pattern of Co_9S_8@NiFe LDH after 20-hrs stability test. High-resolution XPS spectra of Co_9S_8@NiFe LDH after 20-hrs stability test: (b) Co 2p, (c) Ni 2p, (d) Fe 2p, (e) S 2p, (f) O 1s.

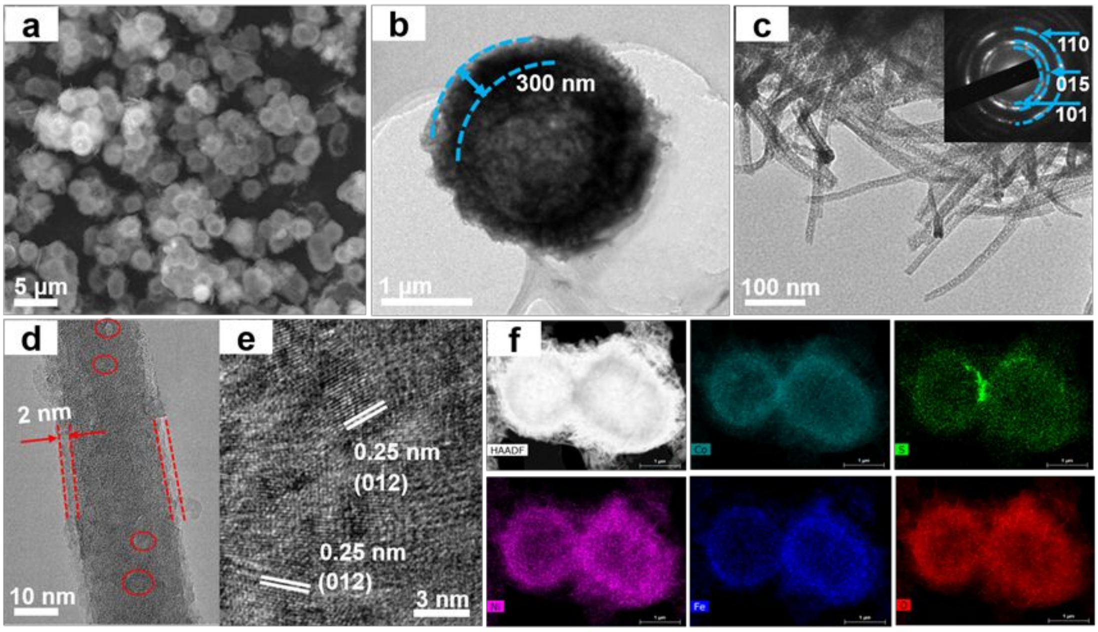

Fig. 5 (a) SEM image of the Co_9S_8@NiFe LDH after 20-hrs stability test. (b) and (c) TEM images of the Co_9S_8@NiFe LDH after 20-hrs stability test (inset of Fig. 5c: SAED of NiFe LDH nanowires in the Co_9S_8@NiFe LDH), (d) and (e) HRTEM images of the Co_9S_8@NiFe LDH after 20-hrs stability test. (f) HAADF-STEM image and EDS mapping of Co, S, Ni, Fe and O from Co_9S_8@NiFe LDH after 20-hrs stability test.

The abundant nanopores in nanowires are shown in Fig. 5d. Such pores offer ample space and effectively buffer structure deformation, which guarantees enhanced stability for OER. Furthermore, a thin NiOOH amorphous layer (2 nm) is observed on the surface of NiFe LDH nanowires. This amorphous layer not only offers more active sites but also prevents the further oxidation of LDH nanowires. The HRTEM image of nanowire in Fig. 5e shows that the lattice spacings of 0.25 nm correspond to the (012) planes of NiFe LDH. EDS mapping in Fig. 5f and Fig. S11 clearly shows an obvious core-shell structure, in which Co, Ni, Fe, S, and O elements are homogeneously distributed. Those results show that constructing NiFe LDH nanowires on the surface of Co_9S_8 hollow spheres to form heterostructures can not only effectively decrease surface oxidation of the Co_9S_8 in Co_9S_8@NiFe LDH but also protect the hollow structure from collapse in this harsh oxidizing environment.

Theoretical investigation of heterointerface effect

The interfacial electronic structure of the Co_9S_8@NiFe LDH composite was investigated using density functional theory (DFT) calculations to better understand the effect of heterointerfaces on enhanced OER activity. These details are described in the Experimental Section. According to the DFT calculation, Co_9S_8 (111) facets have been demonstrated to possess the lowest surface energy.[62] Thus, the most stable (111) facets of Co_9S_8 was used to model the Co_9S_8-NiFe LDH heterostructure. Additionally, the (111) facets of Co_9S_8 and the (001) facets of NiFe LDH show small lattice mismatch ($\approx$5%). Therefore, those two facets were chosen to build the heterointerface. The optimized crystal structures of pure Co_9S_8, pure NiFe LDH, and the interfacial model between Co_9S_8 and NiFe LDH are shown in Fig. S12. The electronic density of states (DOS) curves in Fig. 6a-c show that the bandgap value of pure NiFe LDH is about 1.94 eV. When the NiFe LDH is introduced to the surface of Co_9S_8, the Co_9S_8@NiFe LDH composite has an obviously increased DOS in the vicinity of the Fermi level and exhibits typical metallic property. The partial DOS shows that the Co 3d and S 2p states are responsible for the increased electronic DOS near the Fermi level of Co_9S_8@NiFe LDH. The remarkably enhanced DOS around the Fermi level of Co_9S_8@NiFe LDH explains its high electrical conductivity and high carrier concentration determined by EIS measurements, which reveal that the synergetic effect at the interface results in excellent electron transfer capability. Additionally, the charge redistribution at the Co_9S_8@NiFe LDH interfacial region was analyzed to identify the interlayered electronic interaction between Co_9S_8 and NiFe LDH. According to the Bader charge analysis, about 1.353 electrons are transferred from the NiFe LDH to the Co_9S_8 per unit cell, which aligns well with the XPS analysis (Fig. 6d). The charge redistribution at the interface produces an electron-rich region on Co_9S_8 and a hole-rich region on NiFe LDH, causing the movement of Fermi energy. In addition, the electron transfer from the NiFe LDH to the Co_9S_8 makes Ni and Fe more positively charged, resulting in stronger chemisorption free energies of hydroxides for enhanced OER performance. Both the calculated DOS and the charge difference distribution demonstrate the significant effects of the interface between NiFe LDH and Co_9S_8 on the activity of electrocatalysts.

To better understand the OER activities on the Co_9S_8@NiFe LDH, a detailed OER mechanism was further investigated by DFT calculations (More details in the Supporting Information). Based on the previous research, the OER process consists of four elementary reaction steps, in which *OH is formed from adsorbed OH^- and further oxidizes to *O and *OOH.[63] The schematic illustration of the OER pathway and the optimized structures for the four intermediates involved in each reaction step on the Co_9S_8@NiFe LDH interface and NiFe LDH are shown in Fig. 6e and Fig. S13, respectively. The corresponding free energy diagrams of Co_9S_8@NiFe LDH and

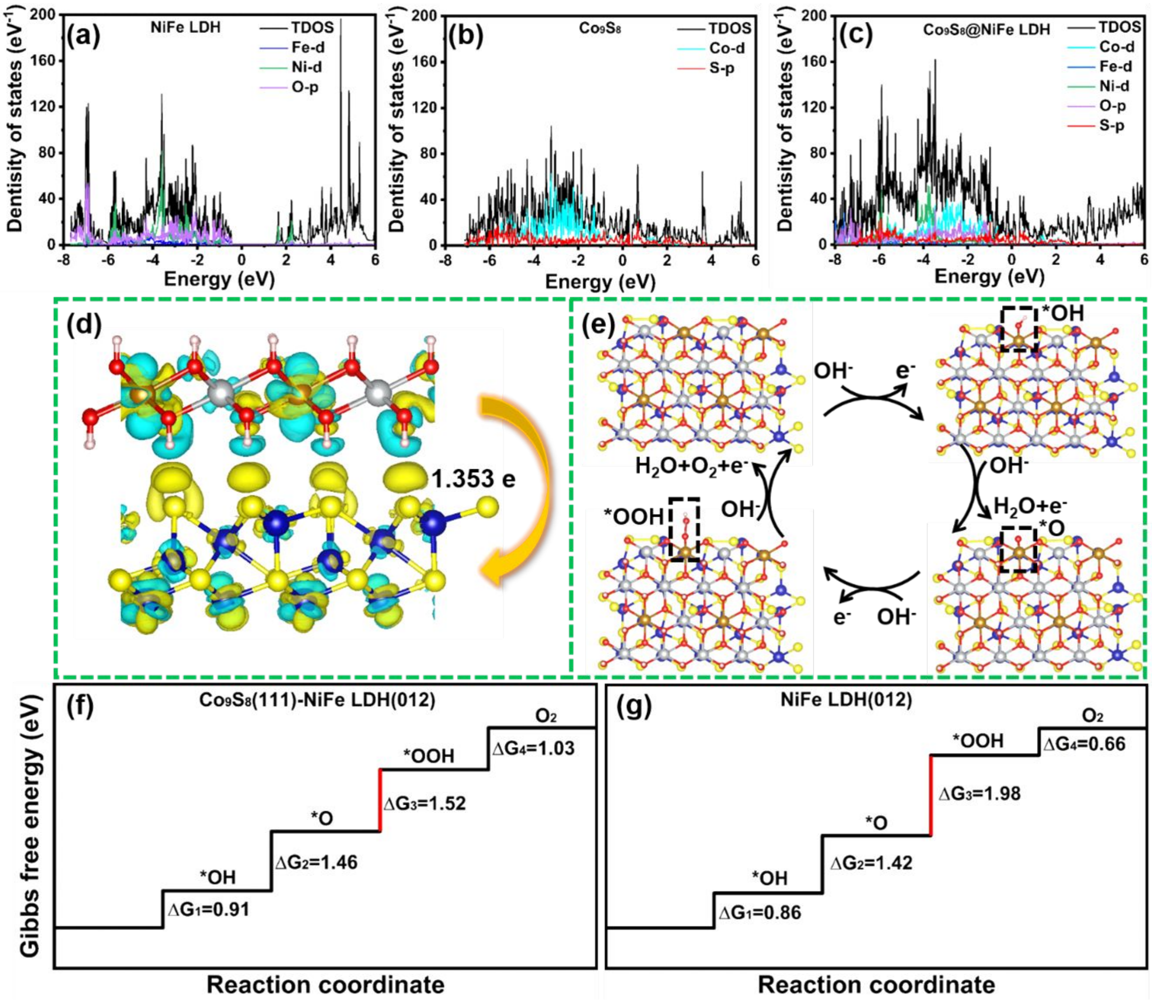

Fig. 6 The density of states (DOS) of (a) NiFe LDH, (b) Co_9S_8 and (c) Co_9S_8@NiFe LDH. (d) Charge density difference at the Co_9S_8@NiFe LDH interface with an isosurface level of 0.002 e/Bohr^3, the yellow and light blue represent the charge accumulation and depletion regions, respectively. Schematic illustration of the OER pathway on the (e) Co_9S_8@NiFe LDH interface and (f) NiFe LDH. The free energy diagram of the OER processes at 0 V on the (g) Co_9S_8@NiFe LDH interface and (h) NiFe LDH.

NiFe LDH for the OER at 0 V are illustrated in Fig. 6f and g. The Gibbs free energies of the four reactions are denoted as ΔG_1, ΔG_2, ΔG_3, ΔG_4, respectively. The calculated values of ΔG_1, ΔG_2, ΔG_3, ΔG_4 for the Co_9S_8@NiFe LDH are 0.91, 1.46, 1.52, 1.03 eV, respectively. In Fig. 6f and g, all reaction steps for OER on both Co_9S_8@NiFe LDH and NiFe LDH are endothermic. The maximized Gibbs free energy step at the equilibrium potential (U=0 V) is the rate-determining step (RDS) and defines the corresponding overpotential for OER ($\eta = (\Delta G_1, \Delta G_2, \Delta G_3, \Delta G_4)_{max}/e{-}1.23$).[20] The *OOH formation from O* with the largest Gibbs free energy is RDS for OER on both Co_9S_8@NiFe LDH and NiFe LDH. The value of ΔG_3 is 1.52 eV with the theoretical overpotential of 0.29 V, which is lower than that of pure NiFe LDH (1.98 eV) with a theoretical overpotential of 0.75 V, suggesting that the heterostructure possesses observably higher intrinsic OER catalytic activity than pure NiFe LDH. Experimental overpotentials depending on the current density are proportional to the theoretical overpotential.[64] According to the above results, the trend of experimental overpotentials for those compounds is very consistent with the theoretical results. The decrease of overpotential in the OER process after introducing NiFe LDH on Co_9S_8 indicates that a synergetic effect between Co_9S_8 and NiFe LDH at the heterointerface plays a crucial role in enhancing OER catalytic performance. The heterointerface between Co_9S_8 and NiFe LDH can optimize the Gibbs free energy of the intermediates and then boost the OER activity.

The superior OER catalytic activity of the Co_9S_8@NiFe LDH can be ascribed to the biphasic and multiscale heterostructure. The as-constructed urchin-like hollow spheres with both micro- and nano scale subunits provide more active sites and super-hydrophilic surfaces to facilitate the adsorption of water-oxidation intermediates, ion penetration, and diffusion of bubbles. The rapid bubble release can effectively boost the utilization of active sites. Meanwhile, the NiFe LDH nanowires can protect the inner Co_9S_8 hollow spheres, providing desired structural stability. The combination of Co_9S_8 with NiFe LDH can modulate the interfacial electronic structure, resulting in the charge transfer from NiFe LDH to Co_9S_8 and excellent electron transfer properties. The heterointerface between Co_9S_8 and NiFe LDH optimizes the Gibbs free energy of the intermediates and possesses lower ΔG for RDS of OER, thus promoting the OER catalytic activity.

Conclusions

In summary, we successfully synthesize urchin-like Co_9S_8@NiFe LDH heterostructured hollow spheres with a diameter of 2.6 µm assembled by one-dimensional nanowires as outer shell and Co_9S_8 hollow spheres as skeletons. As OER electrocatalysts, the Co_9S_8@NiFe LDH illustrates superior OER electrocatalytic activity in 1 M KOH. This system needs an overpotential of 220 mV to deliver a current density of 10 mA cm^{-2} with a low Tafel slope of 52.0 mV dec^{-1}, which is superior to pure Co_9S_8 (282 mV, 57.7 mV dec^{-1}), NiFe LDH (342 mV, 89.0 mV dec^{-1}) and commercial IrO_2 (341 mV, 91.6 mV dec^{-1}). The urchin-like hollow structure with surprising hydrophilicity can facilitate ion penetration and release of bubbles. The strong electronic interactions at the well-defined heterointerfaces can greatly enhance the electron transfer. The DFT calculations show that the synergistic effect at heterointerfaces between Co_9S_8 and NiFe LDH significantly change the RDS and decrease their Gibbs free energy, thus promoting OER catalytic activity. This work provides a new route to prepare composites of other urchin-like hollow sphere structures with high OER performance.

Author Contributions

Xueting Feng: Conceptualization, Methodology, Investigation, Data curation, Writing-Original Draft. Qingze Jiao: Resources, Supervision. Zheng Dai: Methodology. Yanliu Dang: Data curation. Steven L. Suib: Resources, Data curation, Writing-Review & Editing. Jiatao Zhang: Data curation. Yun Zhao: Supervision, Writing-Review & Editing. Hansheng Li: Writing-Review & Editing. Caihong Feng: Resources, Supervision, Writing-Review & Editing. Anlan Li: Data curation, Software, Writing-Review & Editing.

Conflicts of interest

There are no conflicts to declare.

Acknowledgements

This work was supported by the National Natural Science Foundation of China (grant no. 52072034); the US Department of Energy, Office of Basic Energy Sciences, Division of Chemical, Biological and Geological Sciences (grant no. DE-FG02-86ER13622); and the China Scholarship Council (grant no. 201906030038). The computational work for this article was performed on the High Performance Computing Platform at Beihang University.

Notes and references

1 M. S. Dresselhaus and I. L. Thomas, *Nature*, 2001, **414**, 332-337.
2 K. Zhu, F. Shi, X. Zhu and W. Yang, *Nano Energy*, 2020, **73**, 104761.
3 N.T. Suen, S.F. Hung, Q. Quan, N. Zhang, Y.J. Xu and H. M. Chen, *Chem. Soc. Rev.*, 2017, **46**, 337-365.
4 S. Yang, R. Du, Y. Yu, Z. Zhang and F. Wang, *Nano Energy*, 2020, **77**, 105057.
5 D. Dong, Z. Wu, J. Wang, G. Fu and Y. Tang, *J. Mater. Chem. A*, 2019, **7**, 16068-16088.
6 S. Huang, Y. Meng, S. He, A. Goswami, Q. Wu, Junhao Li, S. Tong, T. Asefa and M. Wu, *Adv. Funct. Mater.*, 2017, **27,** 1606585.
7 B.R. Wygant, K. Kawashima and C.B. Mullins, *ACS Energy Let.,* 2018, **3**, 2956-2966.
8 J. Chen, F. Zheng, S.-J. Zhang, A. Fisher, Y. Zhou, Z. Wang, Y. Li, B.-B. Xu, J.-T. and Li, S.-G. Sun, *ACS Catal.,* 2018, **8**, 11342-11351.
9 H. Zhang, X. Li, A. Hähnel, V. Naumann, C. Lin, S. Azimi, S.L. Schweizer, A.W. Maijenburg and R.B. Wehrspohn, *Adv. Funct. Mater.*, 2018, **28**, 1706847.
10 T. Ouyang, Y.-Q. Ye, C.-Y. Wu, K. Xiao and Z.-Q. Liu, *Angew. Chem. Int. Ed.*, 2019, **58**, 4923–4928.
11 Y. Wei, J. Wang, R. Yu, J. Wan and D. Wang, *Angew. Chem. Int. Ed.*, 2019, **58**, 1422–1426.
12 J. Masa and W. Schuhmann, *ChemCatChem*, 2019, **11**, 5842-5854.
13 Y. Wang, S. Tao, H. Lin, G. Wang, K. Zhao, R. Cai, K. Tao, C. Zhang, M. Sun, J. Hu, B. Huang and S. Yang, *Nano Energy*, 2021, **81**, 105606.
14 S. Dou, X. Wang and S. Wang, *Small Methods*, 2019, **3**, 1800211.
15 S. Chen, J. Luo, N. Li, X. Han, J. Wang, Q. Deng, Z. Zeng and S. Deng, *Energy Storage Mater.*, 2020, **30**, 187-195.
16 Y. Hou, M.R. Lohe, J. Zhang, S. Liu, X. Zhuang and X. Feng, *Energy Environ. Sci.*, 2016, **9**, 478-483.
17 Z.-W. Gao, J.-Y. Liu, X.-M. Chen, X.-L. Zheng, J. Mao, H. Liu, T. Ma, L. Li, W.-C. Wang and X.-W. Du, *Adv. Mater.*, 2019, **31**, 1804769.
18 X. Guo, X. Hu, D. Wu, C. Jing, W. Liu, Z. Ren, Q. Zhao, X. Jiang, C. Xu, Y. Zhang and N. Hu, *ACS Appl. Mater. Interfaces*, 2019, **11**, 21506-21514.
19 R. Xu, R. Wu, Y. Shi, J. Zhang and B. Zhang, *Nano Energy*, 2016, 24, 103-110.
20 T. Ouyang, Y.-Q. Ye, C.-Y. Wu, K. Xiao and Z.-Q. Liu, *Angew. Chem. Int. Ed.*, 2019, **58**, 4923–4928.
21 J. Zhang, J. Qian, J. Ran, P. Xi, L. Yang and D. Gao*, ACS Catal.*, 2020, **10**, 12376–12384.
22 X. Feng, Q. Jiao, T. Liu, Q. Li, M. Yin, Y. Zhao, H. Li, C. Feng and W. Zhou, *ACS Sustain. Chem. Eng.*, 2017, **6**, 1863-1871.
23 M.S. Burke, M.G. Kast, L. Trotochaud, A.M. Smith and S.W. Boettcher, *J. Am. Chem. Soc.*, 2015, **137**, 3638–3648.
24 X. Sun, Q. Shao, Y. Pi, J. Guo, X. Huang, *J. Mater. Chem. A,* 2017, **5**, 7769.
25 H. Yang, S. Gao, D. Rao, C. Zhang, X. Zhou, S. Yang, *Sci China Chem*, 2021, **64**, 101-108.
26 G. Kresse, and J. Hafner, *Phys. Rev. B*, 1993, **47**, 558-561.
27 G. Kresse and J. Hafner, *Phys. Rev. B*, 1994, **49**, 14251-14269.
28 G. Kresse, *Phys. Rev. B*, 1996, **54**, 11169-11186.
29 G. Kresse, *Phys. Rev. B*, 1999, **59**, 1758-1775.
30 P. Li, X. Duan, Y. Kuang, Y. Li, G. Zhang, W. Liu and X. Sun, *Adv. Energy Mater.*, 2018, **8**, 1703341.
31 Z. Lu, G. Chen, Y. Li, H. Wang, J. Xie, L. Liao, C. Liu, Y. Liu, T. Wu, Y. Li, A.C. Luntz, M. Bajdich and Y. Cui, *J. Am. Chem. Soc.*, 2017, **139**, 6270−6276.
32 S. Grimme, J. Antony, S. Ehrlich and H. Krieg, *J. Chem. Phys.*, 2010, **132**, 154104.
33 K. Momma and F. Izumi, *J. Appl. Crystal.*, 2011, **44**, 1272-1276.
34 L. Yu, Q. Zhu, S. Song, B. McElhenny, D. Wang, C. Wu, Z. Qin, J. Bao, Y. Yu, S. Chen and Z. Ren, *Nat. Commun*, 2019, **10**, 5106.

35 Y. Ma, Y. Wang, D. Xie, Y. Gu, H. Zhang, G. Wang, Y. Zhang, H. Zhao and P. K. Wong, *ACS Appl. Mater. Interfaces*, 2018, **10**, 6541-6551.

36 J. Guo, Z. Yin, X. Zang, Z. Dai, Y. Zhang, W. Huang and X. Dong, *Nano Res*., 2017, **10**, 405-414.

37 X. Gao, Y. Zhao, K. Dai, J. Wang, B. Zhang and X. Shen, *Chem. Eng. J*., 2020, **384**, 123373.

38 J. Yang, C. Yu, C. Hu, M. Wang, S. Li, H. Huang, K. Bustillo, X. Han, C. Zhao, W. Guo, Z. Zeng, H. Zheng and J. Qiu, *Adv. Funct. Mater*., 2018, **28**, 1803272.

39 J. Jiang, F. Sun, S. Zhou, W. Hu, H. Zhang, J. Dong, Z. Jiang, J. Zhao, J. Li, W. Yan and M. Wang, *Nat. Commun*., 2018, **9**, 2885.

40 J. Liu, J. Wang, B. Zhang, Y. Ruan, L. Lv, X. Ji, K. Xu, L. Miao and J. Jiang, *ACS Appl. Mater. Interfaces*, 2017, **9**, 15364-15372.

41 S. Yin, W. Tu, Y. Sheng, Y. Du, M. Kraft, A. Borgna and R. Xu, *Adv. Mater*., 2018, **30**.

42 W. Liu, J. Zhang, Z. Bai, G. Jiang, M. Li, K. Feng, L. Yang, Y. Ding, T. Yu, Z. Chen and A. Yu, *Adv. Funct. Mater*., 2018, **28**, 1706675.

43 S. Dutta, A. Indra, Y. Feng, T. Song and U. Paik, *ACS Appl. Mater. Interfaces*, 2017, **9**, 33766-33774.

44 L.C. Seitz, C.F. Dickens, K. Nishio, Y. Hikita, J. Montoya, Andrew Doyle, C. Kirk, A. Vojvodic, H.Y. Hwang, Jens K. Norskov and T. F. Jaramillo, *Science*, 2016, **353**, 1011-1014.

45 Y. Luo, L. Tang, U. Khan, Q. Yu, H.-M. Cheng, X. Zou and B. Liu, *Nat. Commun*., 2019, **10**, 269.

46 J. Xiao, A.M. Oliveira, L. Wang, Y. Zhao, T. Wang, J. Wang, B.P. Setzler and Y. Yan, *ACS Catal*., 2021, **11**, 264-270.

47 H. Liu, F.X. Ma, C.Y. Xu, L. Yang, Y. Du, P.P. Wang, S. Yang and L. Zhen, *ACS Appl. Mater. Interfaces*, 2017, **9**, 11634-11641.

48 S. Ju, Y. Liu, H. Chen, F. Tan, A. Yuan, X. Li and G. Zhu, *ACS Appl. Energy Mater*., 2019, **2**, 4439-4449.

49 D. Zhou, S. Wang, Y. Jia, X. Xiong, H. Yang, S. Liu, J. Tang, J. Zhang, D. Liu, L. Zheng, Y. Kuang, X. Sun and B. Liu, *Angew Chem. Int. Ed. Engl.*, 2019, **58**, 736-740.

50 F. Song and X. Hu, *Nat. Commun*., 2014, **5**, 4477.

51 S. Sirisomboonchai, S. Li, A. Yoshida, X. Li, C. Samart, A. Abudula and G. Guan, *ACS Sustain. Chem. Eng*., 2018**, 7**, 2327-2334.

52 X. Xu, H. Chu, Z. Zhang, P. Dong, R. Baines, P.M. Ajayan, J. Shen and M. Ye, *ACS Appl. Mater. Interfaces*, 2017, **9**, 32756-32766.

53 C. Lee, C. Lee, K. Shin, T. Song, H.Y. Jeong, D.Y. Jeon and H.M. Lee, *Catal. Commun*. 2019, **129**, 105749.

54 J.G. Li, H. Sun, L. Lv, Z. Li, X. Ao, C. Xu, Y. Li and C. Wang, *ACS Appl. Mater. Interfaces*, 2019, **11**, 8106-8114.

55 X. Liu, Z. Chen and M. Cao*, ACS Appl. Energy Mater*., 2019, **2**, 5960-5967.

56 S. Deng, Y. Zhong, Y. Zeng, Y. Wang, X. Wang, X. Lu, X. Xia and J. Tu, *Adv. Sci*., 2018, **5**, 1700772.

57 H. Xu, J. Cao, C. Shan, B. Wang, P. Xi, W. Liu and Y. Tang, *Angew Chem. Int. Ed. Engl.*, 2018, **57**, 8654-8658.

58 Y. Zhao, N. Yang, H. Yao, D. Liu, L. Song, J. Zhu, S. Li, L. Gu, K. Lin and D. Wang*, J. Am. Chem. Soc*., 2019, **141**, 7240−7244.

59 Y. Fu, J. Wang, H. Yu, X. Li, H. Wang, J. Tian, R. Yang, *Int. J. Hydrogen Energ.*, 2017, **42**, 20711.

60 S. Li, P. Xu, M.K. Aslam, C. Chen, A. Rashid, G. Wang, L. Zhang and B. Mao, *Energy Storage Mater*., 2020, **27**, 51-60.

61 H. Liang, J. Lin, H. Jia, S. Chen, J. Qi, J. Cao, T. Lin, W. Fei and J. Feng, *J. Power Sources*, 2018, **378**, 248-254.

62 M. Kim, M. A. R. Anjum, M. Choi, H. Y. Jeong, S. H. Choi, N. Park, J. S. Lee, *Adv. Funct. Mater*. 2020, **30**, 2002536.

63 Y. Li, Z. Wang, J. Hu, S. Li, Y. Du, X. Han and P. Xu, *Adv. Funct. Mater*., 2020, **30**, 1910498.

64 M. G. Mota, A. Vojvodic, H. Metiu, I. C. Man, H. Y. Su, J. Rossmeisl and J. K. Nørskov, *ChemCatChem*, 2011, **3**, 1607-1611.